Beyond Butler-Volmer equation for CO_2 electro-reduction on Cu-based gas diffusion electrodes

Peace Adesina[†, ‡], Joel W. Ager [¶, §, ±] and Alexei A. Lapkin [†, ‡, *]

[†]Department of Chemical Engineering and Biotechnology, University of Cambridge, Philippa Fawcett Drive, West Cambridge Site, Cambridge CB3 0AS, United Kingdom

[‡]Cambridge Centre for Advanced Research and Education in Singapore (CARES), CREATE Tower, 1 Create Way, Singapore 138602, Singapore.

[¶]Berkeley Education Alliance for Research in Singapore (BEARS) CREATE Tower, 1 Create Way, Singapore 138602, Singapore.

[§]Chemical Sciences and Materials Science Divisions, Lawrence Berkeley National Laboratory, California 94720, USA.

[±]Department of Materials Science and Engineering, University of California, Berkeley, California 94720, USA

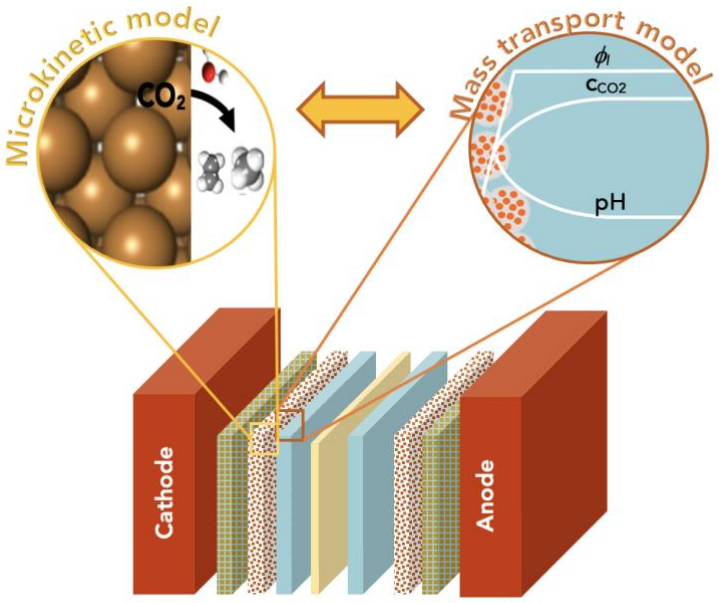

* Corresponding author: aal35@cam.ac.uk

ABSTRACT

We present a methodology for modelling gas diffusion electrodes with Cu-based catalysts. The applicability of the Butler Volmer equation (B-Ve) based on Tafel analysis is limited to single electron transfer reactions which are not typical of CO_2 reduction reactions on Cu catalysts. We developed a method that involves linking the nanoscale effects encapsulated in a detailed calibrated microkinetic model (MKM) on Cu(100) electrodes to a mass transport model (MTM) on a low surface area, flooded agglomerate electrode. The MKM carries richer kinetic information of most reaction pathways described in contemporary literature for Cu(100). Polynomial equations are used to bridge kinetic and transport models without the need for excessive complexity. Our results show that using regression modelling, the microkinetic information at the microscopic level of the catalyst can be successfully linked with the macroscopic electrode models. We observe how mass transport parameters such as CO_2 concentration, pH, and applied voltage, interacts with microkinetic information of the catalyst, influencing the reaction pathways and current densities of key products methane, ethylene, ethanol, and hydrogen. Although the model explores the medium to high voltage regimes, the methodology can address the oversimplification of CO_2 reduction (CO_2RR) kinetics and hydrogen evolution reaction (HER) for observed multiple kinetic regimes if comprehensive microkinetic models are integrated. It also serves as a foundational work for further experimental endeavours for the development of comprehensive microkinetic models. The holistic approach carried out in this work allows for the optimization of both reaction rates and mass transport, paving the way for rational optimisation of electrode designs and their scaling towards commercialization.

***Keywords*:** CO_2 electroreduction; copper gas diffusion electrodes; mass transport; Butler Volmer equation; surrogate modelling; microkinetic model

Notation

Symbol	*Nomenclature*
a	Active specific surface area, m^{-1}
A	Geometric area, m^2
b	Tafel slope, mV dec^{-1}
c_k	Concentration of aqueous species, *k*, mol L^{-1}
d	Diameter, m
D	Diffusivity of species, $m^2\ s^{-1}$
$D_{,eff.}$	Effective diffusivity of species, $m^2\ s^{-1}$
V_0	Equilibrium potential, V
f	Overlapping ratio
F	Faraday's constant (96,500 C mol^{-1})
i	Gas species
J_{lim}	Limiting current density, mA cm^{-2}
j_0	Exchange current density, mA cm^{-2}
$\boldsymbol{J_{SP}}$	Electrode current, mA cm^{-2}
$\boldsymbol{J_{LP}}$	Electrolyte current, mA cm^{-2}
$\boldsymbol{J_{n,SP}}$	Inward electrode current density, mA cm^{-2}
$\boldsymbol{J_{n,LP}}$	Inward electrolyte current density, mA cm^{-2}
J	Current density, mA cm^{-2}
k	Aqueous species
$\boldsymbol{k'}$	Mass transfer coefficient, m s^{-1}
$\boldsymbol{k^0_{sat}}$	Pore saturated permeability of medium, m^2
$\boldsymbol{k_r}$	Pore relative permeability of medium, m^2
$\boldsymbol{L_c}$	Length of cathode, m
M	Molar mass of species g mol^{-1}
M_n	Mean molar mass, g mol^{-1}
n_k	Number of electrons transferred for a specie involved in electrochemical reactions
n_{agg}	Number of agglomerates per catalyst layer
p	Partial pressure of gas, *atm*
P	Total pressure, *atm*
P_0	Initial pressure, *atm*
R	Gas constant (8.314 J $mol^{-1}\ K^{-1}$)
$\boldsymbol{R_k}$	Reaction rate, mol $m^{-3}\ s^{-1}$
$\boldsymbol{S}$	Saturation of porous media
T	Temperature, K
t	Thickness of layer/medium, m
u_g	Darcy velocity of gas mixture, m s^{-1}
u_m	Mobility of species, s mol kg^{-1}
V_0	Equilibrium potential
V_{SP}	Electrode potential, V
V_{agg}	Geometric volume of agglomerate, m^3
w_i	Mass fraction of gas specie in gas mixture, *i*
W_k	Flux of aqueous species, k, mol $m^{-2}\ s^{-1}$
z_i	Charge of participating species, *i*
ε_p	Porosity of medium
ϕ_M	Electrode potential vs PZC, V

ϕ_L	Electric potential in the electrolyte phase, V.
η	Activation overpotential, V
$\propto$	Transfer coefficient
μ_g	Dynamic viscosity of the gas mixture. Pa s
ρ_g	Density of gas mixture, kg m^{-3}
σ_{SP}^{eff}	Effective electrical conductivity of solid phase medium, S m^{-1}
φ	Volume fraction
φ_p	Porosity of catalyst layer
ϕ	Proportion
0	Initial value
agg	Agglomerate
aCL	Agglomerate catalyst layer
CL	Catalyst layer
GDL	Gas diffusion layer
f	Forward reaction
r	Reverse reaction
i	Gas species
K	Liquid species
swe	Swelling
SP	Solid phase
LP	Liquid phase
PTR	Phase transfer reaction
HGR	Homogeneous reaction
ECR	Electrochemical reaction
t	Ionomer thin film thickness
NF	Nafion® ionomer
Cu	Copper nanoparticles
pen	GDL penetration in CL

1. INTRODUCTION

The electrochemical reduction of CO_2 (CO_2RR) is an important and promising CO_2 utilisation technology that can lead to sustainable carbon cycles and the production of valuable fuels and base chemicals for industrial applications. [1–3] Conducting the reaction in vapour-fed cells with gas diffusion electrodes (GDEs) allows the production of higher current densities (>1 A/cm^2) due to the sufficient transport of CO_2 and lower diffusion length by virtue of their lower surface area. [4] However, designing GDEs for optimal current densities and Faradaic efficiencies of desired products is an art due to the plethora of multiscale effects that occur within them. There is no rational framework that links various catalytic multiscale mechanisms such as electrokinetics, mass transport, double layer effects, electrophysical phenomena for Cu electrodes that produce multiple products in one

electrolytic step. This complexity often necessitates meticulous tuning of catalysts. Computational models for CO_2RR on Cu catalysts known to exhibit complex microkinetics from experimental literature still rely on simple and empirically defined electrochemical parameters such as Butler-Volmer Equation (B-Ve).[5] However, the kinetic parameters in B-Ve do not (and cannot) capture the entire reaction network.[6] In this work, we develop a new methodology for incorporating a complex reaction network observed on Cu electrodes, using a 0D microkinetic model coupled with a mass transport model. This paper centres on the method development and shows some preliminary results obtained with the combined model.

2. BACKGROUND

Kinetics are of utmost importance when it comes to understanding the activity of catalysts. In the realm of electrochemical systems, kinetics includes dynamic behaviour of electrodes and electrolytes and rates of electrochemical processes. The typically employed rate coefficient for reactions occurring at metal electrode is the Butler-Volmer equation (B-Ve). The prevailing rendition of the B-Ve equation, often dubbed as the 'Engineer's Butler-Volmer equation' and defined by Eq. 1, is widely adopted in electrochemical models.[7]

$$J = j_0 \left[\exp\left(\frac{(1-\propto)\eta F}{RT} \right) - \exp\left(-\frac{\propto \eta F}{RT} \right) \right] \quad (1)$$

While this relationship is unphysical for certain electrode reactions with reactant mass transport limitations, the concentration dependence of the reactant species can be expressed if the B-Ve is rewritten as Eq. 2.

$$J = j_0 \left[\frac{C_{O\,surf}}{C_{O,ref}} \exp\left(\frac{\propto_a \eta F}{RT} \right) - \frac{C_{R,surf}}{C_{R,ref}} \exp\left(-\frac{\propto_c \eta F}{RT} \right) \right] \quad (2)$$

where, $C_{O\ surf}$ and $C_{O,ref}$ are the concentrations of the oxidized species at the surface and in the bulk solution, while $C_{R,surf}$ and $C_{R,ref}$ are the concentrations of the reduced species at the surface and in the bulk solution. $\propto_a$ and $\propto_c$ are the transfer coefficients of anodic and cathodic reactions.

Two kinetic parameters are defined in the B-Ve: the exchange current (j_0) and the cathodic or anodic transfer coefficient ($\propto$). Exchange current density represents the thermodynamic equilibrium current where the rate of the forward cathodic reaction is equal to the rate of the reverse. In order words, it represents the intrinsic reaction kinetics. These parameters are obtained by conducting electrochemical experiments and fitting them to the B-Ve. The process involves connecting the electrochemical system to a voltage source and measuring the resulting current produced by changing voltage in the positive and the negative directions. A linear region (typically assumed to be the kinetic region) based on Tafel analysis is determined and defined as illustrated in Fig. **1**. This is usually found between the higher voltage (in both forward and reverse directions) and the equilibrium voltage (V_0) and extrapolated back to the equilibrium voltage on the same tangent to give the exchange current density while the slope of that linear line (Cathodic Tafel slope, $b = -\frac{2.303RT}{\propto_c nF}$) carries the value of $\propto$.

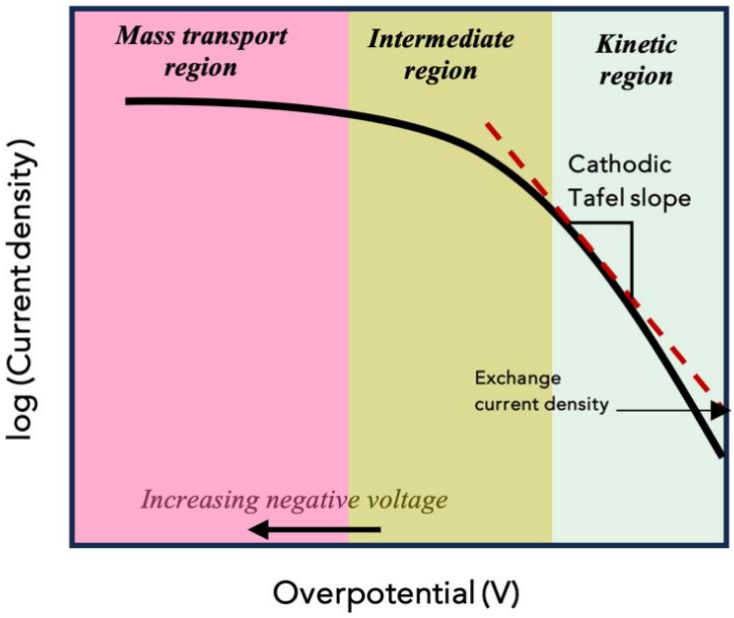

Fig. 1. Determination of kinetic parameters, exchange current density and transfer coefficient for cathodic polarization curves with one kinetic region. The cathodic transfer coefficient ($\propto_c$) is embedded in the determined Tafel slope (*red dotted lines)* and can be obtained from the equation cathodic Tafel slope, $b = -\frac{2.303RT}{\propto_c nF}$. Intermediate or transitional region and mass transport regime are shown.

Eq**. 2** enables the determination of: (*i*) the current density in the kinetically controlled regime, usually obtained at a relatively low activation overpotential and representing the intrinsic reaction rate of the electrocatalyst, and (*ii*) the contribution of the diffusive mass transport limitations for reactants hindered by low solubility and availability, often obtained at higher overpotentials. This introduces nonlinearity of the log(***J***)-V response. Here, the rate of reaction becomes so fast that it is no longer limited by its kinetics. The rate coefficient is so large that the reaction cannot actually proceed at this rate because reactants cannot diffusion fast enough to the reaction site. The latter is found in the limiting current (j_{lim}) region as described by Eq. 3:

$$\frac{1}{J_{tot}} = \frac{1}{j_0 \exp\left(\frac{\eta}{b}\right)} + \frac{1}{j_{lim}} \quad \textbf{(3)}$$

There is another region between the mass transport and the kinetic regions which we refer to as the intermediate or the transitional region, usually omitted in Tafel plots but which contributes to further nonlinearity of the log(***J***)-V response and to the total current density; it is expressed as j_{int} and is shown Fig. **1**. Luckás and Kristóf show that this region holds important data with regards of exchange current of the electrochemical system.[8] Therefore, the total current can be expressed as follows:

$$\frac{1}{J_{tot}} = \frac{1}{j_0 \exp\left(\frac{\eta}{b}\right)} + \frac{1}{j_{int}} + \frac{1}{j_{lim}} \quad (4)$$

Based on the preceding analysis, it becomes evident that determining j_0 and $\propto$ relies on the assumption of a single linear kinetic region, which often proves inaccurate. Typically, this approximation is confined to a narrow potential range around the equilibrium voltage. However, over broader voltage ranges, the assumption of linearity is often invalidated. Microscopically, log(***J***)-V curves exhibit nonlinear electrode kinetics (kinetically limited currents), particularly at higher (negative) voltages, due to the influence of solvent reorganization energy (λ) as per the more rigorous Marcus-Hush-Chidsey (MHC) theory.[6,9–12]

In the utility of linear approximations for log(***J***)-V responses, it is common to encounter multiple kinetic regions covering a broad spectrum of applied voltages, particularly in cases involving complex catalytic activities with multi-step reactions and products.[13] Usually, classification of these regions is left to the expertise and judgement of the researcher. The subjective nature of defining boundaries between these regions for extracting Tafel slopes in log(***J***)-V responses can introduce errors into computational models. Recent studies by Agbo *et al.* and Limaye *et al.* have addressed this issue for a single Tafel slope.[13,14]

Thus, although B-Ve in Eq. **2** provides a framework for analytically elucidating the electrode kinetics, it is fundamentally rooted in empirical observations and assumptions. It is primarily designed for single-electron transfer reactions and certain multistep reactions whose rate-determining step (RDS) is intrinsically much slower than the other steps.[15] Moreso, the applicability of B-Ve can be rather limited in complex electrocatalytic systems with several elementary steps because the overall reaction kinetics are influenced by the factors beyond electron transfer. This is the situation in the case of the cathodic CO_2 reduction reaction (CO_2RR), especially on Cu electrocatalysts, which is the emphasis of this work.

In conducting CO_2RR on copper electrodes, researchers uncovered a fascinating complexity, unveiling the existence of no less than 16 products, which comprise predominantly hydrocarbons amongst a diverse array of alcohols, aldehydes, ketones, and carboxylic acids.[16] The mechanistic routes leading to the formation of these products on copper reveal that certain pathways are activated by availability of protons, electrons or a concerted/sequential proton and electron transfer processes and potential.[16–18] Other factors, such as the coverage of reactants/intermediates, multiple competing reaction pathways, surface adsorption/desorption kinetics and additional chemical reaction steps (typically from side reactions), introduce complexity to the identification of a definitive RDS. This complexity is further exacerbated by the influence of the catalyst particles facet structure and surface reconstruction on product selectivity.[18–23]

Experimental observations of CO_2RR reveal that conventional concept of a single Tafel slope is inadequate in explaining the electrode activity of certain products generated on Cu electrocatalysts for the CO_2RR.[14] Therefore, using exchange current density and Tafel slopes to predict current densities is often inaccurate. Figs. **2a** and **2b** illustrate multiple distinct kinetic regions for typical log(***J***)-V responses of a hydrocarbon product specie and hydrogen product specie respectively. The multiple kinetic regions arise from the complex nature of multi-step reactions, the interlocking relationship between the CO_2RR and side reactions, such as HER and the formation of various heterogenous products, where coverage of reactive intermediates is dependent on the electrode potential, surface concentrations of reactants, and local pH.

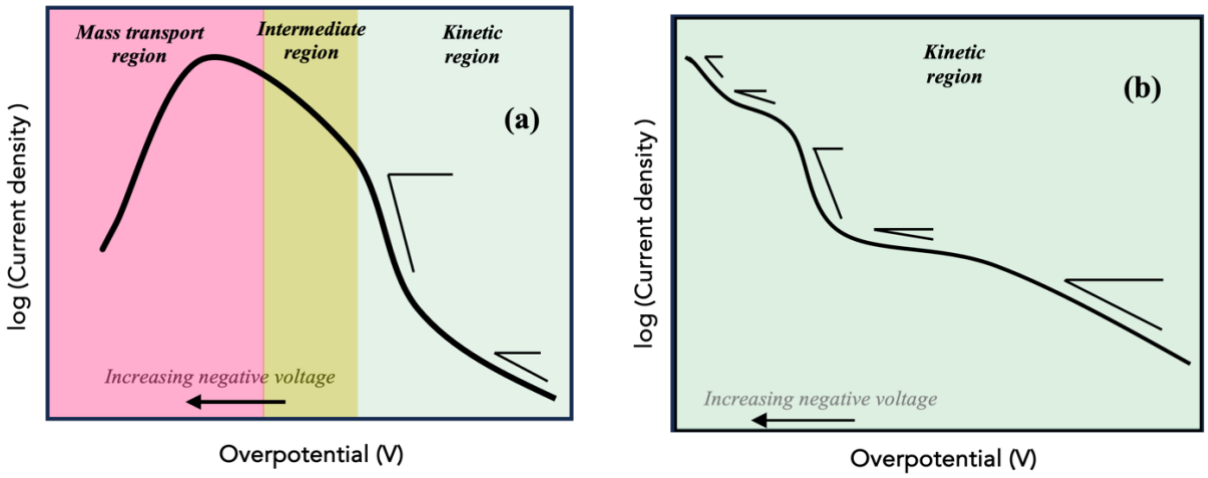

Fig. 2. (a) An overall illustration of multiple regimes in CO_2RR reaction, including several kinetic regions, an intermediate regime and mass transport regime. **(b)** A more detailed illustration of multiple kinetic regions for competing hydrogen evolution reaction (HER) producing hydrogen; there is no mass transport limitation due to the availability of reactant.

In the CO_2RR literature, it has been observed that as applied voltage changes, distinct voltage regions emerge in which reaction mechanism transitions from one dominant pathway to another. In fact, Tafel slope is dependent on the applied voltage and specie surface coverage. For instance, in the case of Cu_2O – derived Cu catalysts, Huang *et al* discovered that ethylene production is notably enhanced at a voltage of -0.98V *vs* RHE, while methane generation is reduced at -1.13 V *vs* RHE.[18] Production of ethylene was observed when production of CO plateaued at -0.63 V *vs* RHE. This indicates the switch from one kinetic regime to another, orchestrated by specific applied voltages and coverage, or pH, for which a particular product formation becomes prevalent within a voltage region.

Similarly, in the context of H_2 production, multiple Tafel regions are observed. Initially, H_2 production prevails at low overpotentials, typically -0.3 V and -0.6 V *vs* RHE. This is attributed to the fact that the necessary potential for catalysing CO_2 reduction has not been reached. However, as overpotential increases, the dominance of H_2 temporarily diminishes due to the prevailing CO_2RR

activity blocking active sites that promote HER and suppressing the side reaction. Subsequently, at even higher overpotentials, H_2 production shows a resurgence.[18]

The presence of multiple kinetic regimes, as observed in Figs. **2a** and **2b**, requires the generation of several Tafel plots to effectively capture these variations.[13] This results in the classification of different coverage dependent Tafel regions (since coverage varies with voltage), each characterised by its specific exchange current density and transfer coefficient. To accurately establish Tafel slopes that vary with surface coverage, it is imperative to employ rigorous microkinetic models instead of simpler models that make use of conventional assumption of terminal coverages of $\theta = 1$ or $\theta = 0$ as pointed out by Shinagawa *et al.*[24] This approach can be quite complex due to the considerable influence exerted by CO* surface coverage on the energy barrier associated with C-C coupling for C2 intermediates.[25,26] Also, the possibility of overlapping Tafel plots poses challenges in distinguishing between various kinetic regimes and accurately determining kinetic parameters.

Instead of categorizing and defining Tafel regions, our study explores the development and utilisation of comprehensive and calibrated microkinetic models on CO_2RR planar electrode or GDE models. Microkinetic models have been known to offer a consistent framework for analysing individual reaction mechanisms and identifying critical essential elements such as the rate-determining step and predominant surface species involved in the reaction.[27] Therefore, when they are directly integrated with reactor level models (such as a GDE mass transport model), they provide a route to rational design of GDEs. This ensures the preservation of essential kinetic details that would otherwise have been lost if simplified to fit a specific kinetic framework such as B-Ve, which is not natively applicable to complex electrochemical reactions.

In this study, we adopt a detailed calibrated microkinetic model developed by Rihm *et al.*, which accounts for all proposed reaction pathways and elementary steps in the CO_2RR literature on Cu(100)

surfaces.[28] The calibrated model ensures consistency with thermodynamic calculations and experimental findings, while also aligning with the accuracy of *ab initio* calculations.[28] We further discuss the microkinetic model in Section **2.5**. We invite readers to read the work of Rihm *et al*. for details of the microkinetic model for CO_2 reduction on Cu electrodes.[28] For this work, we explore and develop a methodology for coupling mass transport and microkinetic models.

Some of the benefits of direct coupling of a microkinetic model with a continuum mass transport model is to alleviate the challenges associated with fitting several Tafel slopes to B-Ve or its variants. In the coupled model, the species current density is supplied by a microkinetic model, taking input of mass transport parameters from the mass transport model. This self-consistent methodology allows to build comprehensive understanding of how mass transport influences reaction kinetics on Cu electrodes.

Further, the methodology eliminates the necessity of developing rigorous computational frameworks for extraction of kinetic parameters for multiple Tafel slopes. Additionally, it alleviates the need to develop modified and expanded versions of the Butler-Volmer equation (B-Ve) to capture the intricacies of the specific reactions. By doing so, unnecessary parameterization is avoided.

2. COMPUTATIONAL DETAILS

A 1D model was constructed with two functional layers, which include the gas diffusion layer (GDL) with a thickness of 325 μm and an agglomerate catalyst layer (*a*CL) with a thickness depending on the mass loading of composite materials comprising the layer. This is described schematically in Fig. **3.**

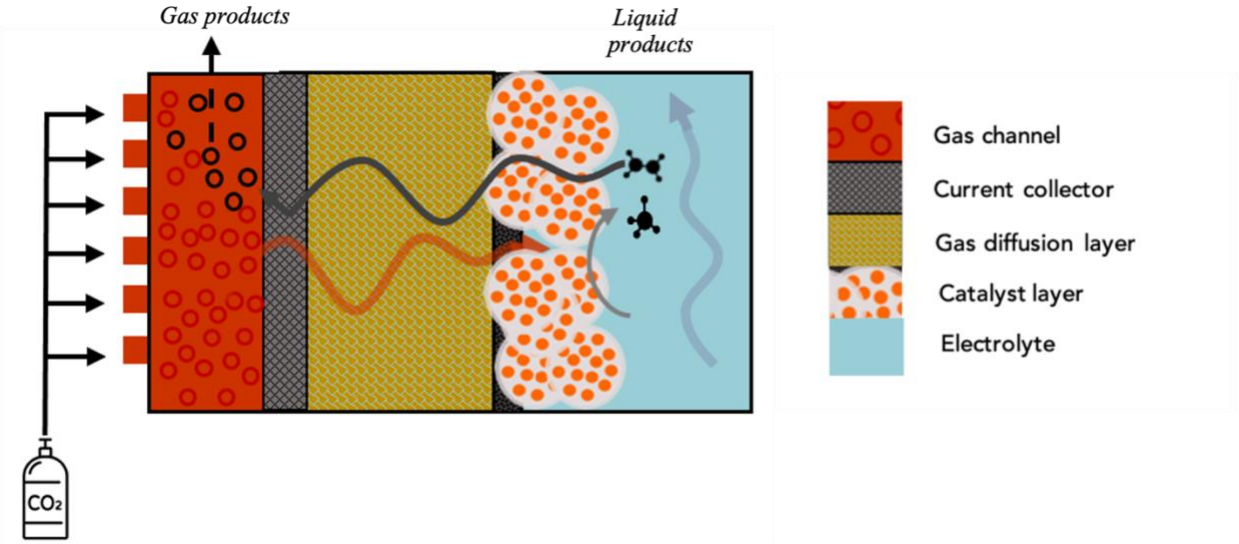

Fig. 3. Schematics of a gas diffusion electrode (*not drawn to scale*).

A total of 15 ionic, reactant and product species are modelled in this work. To reduce computational cost and mitigate the risk of encountering convergence problems, in addition to six species from the side bicarbonate reactions in the catholyte (CO_2, H^+, OH^-, K^+, CO_3^{2-}, HCO_3^-), we explore only on 9 CO_2RR products with substantial current densities, as shown in Table **1**. The catholyte and its concentration is 0.1 M $KHCO_3$. Physical parameters of the GDE and physical properties of the participating species enumerated in **Table 1** are given in **Tables S1** and **S2** in the Supporting Information.

The homogenous reactions taking place between CO_2 and H_2O/OH^- are included in the reaction term (Eq. 5 – 9). Values of the forward and the reverse rate constants are given in the Supporting Information **Table S3**.

$$CO_{2(aq)} + H_2O \overset{k_{1f},k_{1r}}{\Longleftrightarrow} H^+ + HCO_3^- \qquad K_1 = 4.27 \times 10^{-7} \qquad (5)$$

$$HCO_3^- \overset{k_{2f},k_{2r}}{\Longleftrightarrow} H^+ + CO_3^{2-} \qquad K_2 = 4.79 \times 10^{-11}\ \text{M} \qquad (6)$$

$$CO_{2(aq)} + OH^- \overset{k_{3f},k_{3r}}{\Longleftrightarrow} HCO_3^- \qquad K_3 = 4.44 \times 10^{7}\ \text{M}^{-1} \qquad (7)$$

$$HCO_3^- + OH^- \overset{k_{4f},k_{4r}}{\Longleftrightarrow} H_2O + CO_3^{2-} \qquad K_4 = 4.66 \times 10^{3}\ \text{M}^{-1} \qquad (8)$$

$$H_2O \overset{k_{5f},k_{5r}}{\Longleftrightarrow} H^+ + OH^- \qquad K_W = 10^{-14}\,\mathrm{M}^2 \qquad (9)$$

Table 1. Cathodic reactions included in the model.

Products	Reactions
Carbon monoxide	$CO_{2(g)} + H_2O + 2e^- \leftrightarrow CO_{(g)} + 2OH^-$
Formate	$CO_{2(g)} + H_2O + 2e^- \leftrightarrow HCOO^-_{(l)} + OH^-$
Formaldehyde	$CO_{2(g)} + 3H_2O + 4e^- \leftrightarrow CH_2O_{(g)} + 4OH^-$
Methanol	$CO_{2(g)} + 5H_2O + 6e^- \leftrightarrow CH_3OH_{(l)} + 6OH^-$
Methane	$CO_{2(g)} + 6H_2O + 8e^- \leftrightarrow CH_{4(g)} + 8OH^-$
Acetate	$2CO_{2(g)} + 5H_2O + 8e^- \leftrightarrow CH_3COO^-_{(l)} + 7OH^-$
Ethylene	$2CO_{2(g)} + 8H_2O + 12e^- \leftrightarrow C_2H_{4(g)} + 12OH^-$
Ethanol	$2CO_{2(g)} + 9H_2O + 12e^- \leftrightarrow C_2H_5OH_{(l)} + 12OH^-$
Hydrogen	$2H_2O + 2e^- \leftrightarrow H_{2(g)} + 2OH^-$

2.1 Model Assumptions

The main features and assumptions of the model are explicitly described below:

1. ***Reaction conditions*:** Isothermal, steady state conditions and ideal gas behaviour are assumed in this model. The GDE model is operated at 1 atm and 298 K (25 °C).

2. ***Reactant gas transport in GDE***: Feed gas is introduced into the gas channel chamber with a composition of 98% CO_2, 1% CO and 1% H_2 by mole. Ideal gas conditions are assumed for the feed gases. The reactant gases are transported by diffusion and convection through the GDL to the *a*CL where the reaction occurs. Transport is described by the mixture-averaged diffusion model as shown in **Table 2**.

3. ***Structure of the catalyst layer***: Nafion®, a perfluorinated sulfonic acid ionomer (PFSA)-based membrane, is commonly added to catalyst mixture as a supporting material to enhance catalyst dispersion. However, owing to its binding properties, the catalysts are prone to aggregation and overlapping, drastically reducing active surface area. In our modelling approach, we treat the catalyst as flooded agglomerates, considering them to be overlapping spherical structures with a thin film of ionomer around them as shown in Fig. **3.**

We assume that these agglomerates exhibit homogeneity and are uniformly distributed within the catalyst bed, creating new macro-porosity between each agglomerate. Furthermore, we hypothesize that when electrolyte reaches the Nafion®-filled agglomerate, it is adsorbed by Nafion®, causing it to swell till it reaches saturation of 0.78. Structural characterisation of the agglomerate catalyst layer is described in **Section 2.3**.

4. ***Aqueous ion transport in aCL*:** The aqueous electrolyte supplies mobile ions to the *a*CL, where the reaction occurs. Transport of ions within *a*CL is described by the Nernst Planck equations given in Table 3. We assume electroneutrality in the *a*CL domain due to the longer length scale of CL, in the order of microns, compared to the nanometre length scales where the ion effects are pronounced.[29]

5. ***Donnan exclusion forces in Nafion® and impact on product selectivity*:** Nafion® is known for its ion exchange properties, allowing selective and restrictive transport of counterions and co-ions respectively. This impacts transport and concentration of H^+ and OH^- ions in the local microenvironment of catalytic sites due to the residing negative charges, and favours formation of some products over others.[30,31] The components of the catalyst ink that use Nafion® ionomer also affect product selectivity of the reaction. However, while this is very important, we do not

account for these observed effects in our model due to lack of data in the literature on these effects on Cu electrodes.[32,33] There is still limited understanding on the impact of Nafion® on product selectivity with regards to reaction mechanistic pathways that are accessible or inaccessible due to their energy barriers.

2.2 Governing Equations

The conservation equations, source term equations, boundary conditions of gas and ions transport through the functional layer that makes up the GDE (i.e., GDL and CL) are given in Tables **2**-**5**.

Table 2. Conservation equations of gas transport in the functional layers of the GDE.

Variables	Equations	Eq. no	Functional layer
Gas transport			
Gas flux	$\frac{\partial}{\partial t}(\varphi_p \rho_g) + \nabla \cdot (\rho_g u_g) = R_{PTR}$	(10)	GDL, CL
Mass-averaged gas velocity	$u_g = \frac{K_P}{\mu_g} \nabla P$	(11)	GDL, CL
Inlet gas mass fractions	$\left(\rho \frac{\partial w_i}{\partial t}\right) + \nabla \cdot J_i + \rho (u_g \cdot \nabla) w_i = R_{PTR}$	(12)	GDL, CL
Gas mass flux	$J_i = -\left(\rho D_i^{eff} \nabla w_i + \rho w_i D_i^{eff} \frac{\nabla M_n}{M_n}\right)$	(13)	GDL, CL
Bruggeman's Model	$D_i^{eff} = D_i \varphi_p{}^{1.5}$	(14)	GDL
	$D_i^{eff} = D_i \varphi_{p,swe}{}^{1.5}$	(15)	CL
Total diffusion	$D_i = \frac{1}{\frac{1}{D_i^M} + \frac{1}{D_i^{KN}}}$	(16)	GDL, CL
Molecular Diffusion	$D_i^M = \frac{1 - w_i}{\sum_{x \neq i}^{N} \frac{x_x}{D_{ix}}}$	(17)	GDL, CL
Knudsen Diffusion	$D_i^{KN} = \frac{d_{pore}}{3} \sqrt{\frac{8RT}{\pi M_i}}$	(18)	GDL, CL
Average molar mass of inlet gas mixture	$M_n = \frac{1}{\sum_i \frac{w_i}{M_i}}$	(19)	GDL, CL

Pore Permeability	$k_m^{eff} = k_{sat}\ k_r$	(20)	GDL, CL
	$k_{sat} = k_{sat}^0 \frac{\varphi_p^3}{(1-\varphi_p)^2}$	(21)	GDL
	$k_{sat} = k_{sat}^0 \frac{\varphi_{p,swe}^3}{(1-\varphi_{p,swe})^2}$	(22)	CL
	$k_r = (1-S)^3$	(23)	GDL, CL

Table 3. Conservation equations of liquid transport in the functional layers of the GDE.

Variables	Equations	Eq. no	Functional layer
Liquid transport			
Concentration of aqueous ions	$\frac{\partial \varepsilon_l c_k}{\partial t} + \nabla \cdot J_K = \varepsilon_l (R_{HGR} + R_{ECR} + R_{PTR})$	(24)	CL
Ion flux/ Electroneutrality assumption	$J_k = -D_K^{eff} c_K - z_K u_{m,K} F c_K \nabla \phi_{LP}$	(25)	
	$\sum_k z_K c_K = 0$	(26)	CL
Electron transport			
Electric current density	$\nabla \cdot J_{SP} = -a_{CL} \sum_k J_K$	(27)	CL
	$J_{SP} = -\sigma_{SP}^{eff} \nabla V_{SP}$	(28)	CL

Table 4. Source term for the functional layers in the GDE.

Reactions	Equations	Eq. no	Functional layer
Gas phase			
Gas phase transfer reaction	$R_{PTR,CO2} = -\frac{a_{CL} D_{CO2}\, \phi_{NF,aq} M_{CO2}}{t_{NF}} (H_{CO2,s} p_{CO2} - c_{CO2})$	(29)	CL
Aqueous phase			
Electrochemical reactions	$\boldsymbol{R}_{ECR,j} = M_K \sum_k \frac{a_{CL} s_{j,K} \boldsymbol{J_K}}{n_K F}$ *where K are the dissolved reactant and product species listed* CO_2, CO, $HCOO^-$, CH_4, C_2H_4, C_2H_6, CH_2O, C_2H_4, CH_3OH, C_2H_5OH, CH_3COO^-	(30)	CL
Homogeneous reactions	$\boldsymbol{R}_{HGR,CO2} = -k_{1,f}[CO_2] + k_{1,r}[HCO_3^-][H^+] - k_{3,f}[CO_2]\,[OH^-] + k_{3,r}[HCO_3^-]$	(31)	CL
	$\boldsymbol{R}_{HGR,CO3} = k_{2,f}[H^+][CO_3^{2-}] - k_{2,r}[HCO_3^-] + k_{4,f}[HCO_3^-][OH^-] - k_{4,r}[CO_3^{2-}]$	(32)	CL
	$\boldsymbol{R}_{HGR,HCO3} = k_{1,f}[H^+][HCO_3^-] - k_{1,r}[CO_2] - k_{2,f}[H^+][CO_3^{2-}] + k_{2,r}[HCO_3^-] + k_{3,f}[CO_2][OH^-] - k_{3,r}[HCO_3^-] - k_{4,f}[HCO_3^-][OH^-] + k_{4,r}[CO_3^{2-}]$	(33)	CL
	$\boldsymbol{R}_{HGR,H} = k_{1,f}[CO_2] - k_{1,r}[HCO_3^-][H^+] + k_{2,f}[HCO_3^-] - k_{2,r}[CO_3^{2-}][H^+] + k_{5,f} - k_{5,r}[H^+][OH^-]$	(34)	CL
	$\boldsymbol{R}_{HGR,OH} = -k_{3,f}[CO_2][OH^-] + k_{2,r}[HCO_3^-] - k_{4,f}[HCO_3^-][OH^-] + k_{4,r}[CO_3^{2-}] + k_{5,f} - k_{5,r}[H^+][OH^-]$	(35)	CL

Table 5. Boundary conditions.

Variables	CC/GDL	GDL/CL	CL/Electrolyte	Eq. no
Gas transport				
Inlet gas Pressure	$\mathbf{P = P_0}$	-	-	(36)
Inlet gas mass fractions	$w_{0,co2} = 0.98$ $w_{0,H2} = 0.01$ $w_{0,CO} = 0.01$	-	-	(37)
Liquid transport				
Ion flux	-	-	$N_K = k_K{}'(c_K^{bulk} - c_K)$	(38)
Mass transfer coefficient			$k_k{}' = \frac{\overline{Sh_x} D_K}{L_{elec}} = \left(\frac{D_K}{L_c}\right) 0.664 \left(\frac{\rho_l u_l L_c}{\mu_l}\right)^{0.5} \left(\frac{\mu_l}{\rho_l D_K}\right)^{0.333}$	(39)
Electrode potential	$V_{SP} = -0.85\,V \; - \; -1.27\,V$	-	-	(40)
Electrolyte potential	-	-	$V_{LP} = 0$	(41)
Electrode current density	-	-	$-\boldsymbol{n} \cdot \boldsymbol{J_{SP}} = \boldsymbol{J_{n,SP}}$ $\boldsymbol{J_{SP}} = \mathbf{0}$	(42)
Electrolyte current density	-	$-\boldsymbol{n} \cdot \boldsymbol{J_{LP}} = \boldsymbol{J_{n,LP}}$ $\boldsymbol{J_{LP}} = \mathbf{0}$	-	(43)

2.3 Agglomerate model and surface area characterisation

The agglomerate catalyst consists of copper catalyst particles, Nafion® ionomer, void spaces between the agglomerated catalyst particles, and the penetrated GDL into the *a*CL.[34] The mass loadings of copper and ionomer and the corresponding densities can be used to calculate their volume fractions.

We assume that thickness of the catalyst is constant; thus, porosity of the CL can be determined from Eq. 44 after substitution of Eqs. 45 – 47. Furthermore, Nafion® is known to absorb water and swell; the corresponding reduction in porosity of the CL is accounted for in Eq. 48.

$$\varphi_p = 1 - \varphi_{Cu} - \varphi_{NF} - \varphi_{pen} \tag{44}$$

$$\varphi_{Cu} = \frac{m_{Cu}}{\rho_{Cu} t_{CL}} \tag{45}$$

$$\varphi_{NF} = \frac{m_{NF}}{\rho_{NF} t_{CL}} \tag{46}$$

$$\varphi_{pen} = \phi_{GDL}\,(1 - \varphi_{GDL}) \tag{47}$$

$$\varphi_{p,\,swe} = \varphi_p - \varphi_{NF} k_s \lambda \tag{48}$$

The corrected porosity (Eq. 48) illustrates the extent to which the agglomerates within the catalyst layer overlap with one another. The overlap of agglomerates reduces the active surface area available for catalytic reactions.

To calculate the active surface area of a catalyst, first geometric specific surface area of one agglomerate is found according to Eq. 49.

$$a_{agg} = \frac{A_{agg}}{V_{agg}} = \frac{4\pi {R_{agg}}^2}{\frac{4}{3}\pi {R_{agg}}^3} = \frac{3}{R_{agg}} \tag{49}$$

Then, the number of agglomerates within the catalyst layer is calculated by dividing the volume of catalyst layer by the geometric volume of a single spherical agglomerate corrected for swelling of Nafion® within the catalyst layer.

$$n_{agg} = \left(1 - \varphi_{p,\,swe}\right)\frac{V_{CL}}{V_{agg}} \tag{50}$$

The specific surface area of the catalyst layer is obtained by multiplying both sides of Eq. 50 by the geometric area of one agglomerate, A_{agg} and dividing by the volume of catalyst layer.

$$\frac{n_{agg}A_{agg}}{V_{CL}} = \left(1 - \varphi_{p,\,swe}\right)\frac{A_{agg}}{V_{agg}} \tag{51}$$

$$a_{CL} = \left(1 - \varphi_{p,\,swe}\right)a_{agg} \tag{52}$$

The focus of this work is on the overlapping agglomerate particles. We utilise the derivation of the overlapping ratio, *f*, and the effective surface area of the catalyst layer, denoted as a_{CL}, proposed by Cetinbas *et al.* given by Eqs. 53 and 54. [35]

$$\left(\frac{m\pi}{24\left(1 - \varphi_{p,\,swe}\right)\alpha_m} + 1\right)f^3 - 3\left(\frac{m\pi}{24\left(1 - \varphi_{p,\,swe}\right)\alpha_m} + 1\right)f^2 +$$

$$3f + \left(\frac{\pi}{6\left(1 - \varphi_{p,\,swe}\right)\alpha_m} - 1\right) = 0 \tag{53}$$

$$a_{CL} = \frac{\pi}{\alpha_m D_p(1-f)^2}\left[1 - \frac{mf}{2}\right] \quad \text{for} \quad \varphi^0_{p,\,swe} \leq \varphi_{p,\,swe} \leq \varphi^{cr}_{p,\,swe} \tag{54}$$

A rhombohedral packing density of an agglomerate is assumed with characteristics such as the number of contact points, critical porosity, packing density shown in **Table 6.** Therefore, the overlapping ratio, *f*, is determined from Eq. 53 and the calculated porosity of the swollen catalyst layer $\varphi_{p,\,swe}$ in Eq. 48.

The estimated value of *f* should be the smallest root value after solving the cubic polynomial in Eq. 53. The value of the overlapping ration, *f*, is substituted into Eq. 54 to calculate the specific surface area of the catalyst layer. **Table 6** contains other details and values of parameters used to develop the agglomerate model.

Table 6. The agglomerate model and surface area properties.

Variables	Symbols	Value	Unit	Reference
Mass loading of Cu catalysts	m_{Cu}	2.0	mg cm^{-2}	Assumed
Mass loading of Nafion® ionomer	m_{NF}	0.5 – 0.7	mg cm^{-2}	Assumed
Ratio of mass loading of Cu to Nafion®	m_{ratio}	2.86 – 4	-	-
Diameter of copper nanoparticles	D_p	25	*nm*	-
Proportion of GDL infiltration in CL	ϕ_{GDL}	0.15	-	Assumed
Thickness of CL	t_{CL}	6	μm	Assumed
Radius of agglomerate	R_{agg}	10^2	μm	Assumed
Ionomer swelling coefficient	k_s	0.0126	-	[34]
Ionomer water content	λ	20	-	[34]
Density of dry Nafion® ionomer	ρ_{NF}	2.0	g cm^{-3}	[34]
Density of copper	ρ_{Cu}	8.96	g cm^{-3}	-
Number of contact points	m	12	-	[35]
Critical porosity	$\varphi^{cr}_{p,\,swe}$	0.2595	-	[35]
Packing factor	α_m	0.7071	-	[35]
Critical overlapping porosity	$\varphi^{0}_{p,\,swe}$	0.0359	-	[35]
Thickness of Nafion®	t_{NF}	400	nm	Assumed

2.5. **Microkinetic model**

Integration of microkinetic analysis into reactor-level models, such as gas diffusion electrode (GDE) models, serves the dual purpose of elucidating the intricate reaction mechanisms

involved in the electrocatalytic reduction of CO_2 and facilitating the upscaling of these insights to the macroscopic scale. This is because kinetic parameters governing the elementary steps correspond to formation and breaking of chemical bonds, which occur at a microscale level.[36]

Given the complexity of the reaction on Cu electrodes, a rigorous approach is adopted rather than selecting a limited number of presumed key reaction mechanisms, as has been done in recent literature.[5,37,38] The microkinetic model employed in this study encompasses a broad reaction network, incorporating possible feasible and commonly observed elementary reaction events documented on Cu(100), an extensively studied facet in Cu electrocatalysis for CO_2 reduction, sourced from a variety of experimental and *ab initio* studies.[39–45] The interactions among these steps contribute to the development of the predominant catalytic reaction mechanism amounting to 77 functional reaction elementary steps.[28]

Both the continuum and microkinetic models allow for effective capture of temporal changes in reaction rates and species concentrations on the electrode. However, in our case, the use of different software tools for developing the microkinetic model and the mass transport model posed a challenge in coordinating their integration within the same time interval. The mass transport model was developed in COMSOL Multiphysics 6.0, while the microkinetic model was developed using Cantera libraries, compiled with Cantera C++ library. The pre-processing and input files to the microkinetic model were developed in Python. Consequently, we opted to develop steady-state mass transport and microkinetic models as a pragmatic solution. Since the microkinetic model is transient with a last time step of 2,400 s, current densities corresponding to the last time step are taken to be the steady state current densities of product species and were used in the mass transport model. Nonetheless, future research could explore

the development of dynamic models for both mass transport and micro-kinetics, provided that effective management of time intervals can be achieved.

The full reaction network and the elementary steps are shown in Fig. S1 and Table S5 in the Supporting Information. The list of products that are considered in this network are shown in Tab**le 1**. The network includes adsorption of reactants, surface transformation reactions through hydrogenation steps, coupling of C1-C1 intermediates to form C2 products or a combination of hydrogenation and coupling steps and desorption of products.[28]

In the development of the calibrated microkinetic model, a kinetic model was initially formulated considering Gibbs free energies, activation barriers, pre-exponential factors and charge transfer coefficients for each of the considered elementary reaction in the reaction network. These parameters are provided with appropriate uncertainty ranges and target values from *ab initio* DFT calculations conducted in literature. By optimizing the experimental values of these parameters using the Hooke Jeeves algorithm against the objective function of the theoretical bounds derived from *ab initio* calculations in literature, the model ensures calibration with anticipated theoretical calculations for each elementary reaction. Other sequential optimisation towards logarithmic scaled Faradaic efficiencies addressing stoichiometric, thermodynamic, and kinetic consistency of each elementary reaction including sensitivity analysis, were undertaken to further calibrate the microkinetic model for Cu(100) single crystals.[28]

Since the microkinetic model was calibrated towards experimental Faradaic efficiencies instead of experimental partial current densities, the current densities were subsequently back calculated. This is because Faradaic efficiency scaling offers a simpler and more manageable

approach for model calibration compared to directly calibrating towards current density especially at higher voltages. At higher voltages, increased catalytic activities are observed as several other minor products are formed – thereby posing some challenges in capturing all these products in a calibrated microkinetic model. Future microkinetic model should target species current density values as they are more useful in reactor level models.

For the present model, we have chosen to restrict the reaction network model to the most well-studied mechanistic pathways associated with Cu (100) surface. This surface is dominating in polycrystalline copper particles. At the same time, we acknowledge that under specific reaction context (temperature, fluids composition, electrode potential, support material and nanoparticle size) there exist certain distribution of facets on an active catalyst. While there is a continuing debate on mechanistic pathways on different Cu surfaces, the extension of the model to the distribution of facets and a more complex model of a distribution of reaction networks is beyond the scope of this work.[46]

The use of nanostructured catalysts results in different roughness factors (RFs), which represent the ratio of the electrochemical active surface area (ECSA) to the geometric electrode area (GESA). In this work, we looked at the increased number of sites as it pertains to GDEs rather than the intrinsic catalytic activity (average turnover frequency). Therefore, nanocatalysts with different roughness factors (surface areas) will achieve mass transport limitations at different rates. The surface area of a GDE is directly linked with its surface pH (local pH) of the porous catalytic bed due to the increased production of OH^- ions from increased active sites.

2.4. **Combining mass transport and microkinetic models**

Scheme 1 illustrates the methodology of combining the GDE mass transport model with the kinetic model. These models were developed using different software packages, resulting in a mismatch in time-stepping intervals and data formats. This discrepancy posed synchronisation challenges and data transfer/retrieval errors. To address this, a polynomial approximation of the species current density ($\boldsymbol{J}_K$) containing three major independent variables as described by the microkinetic model data, was employed to facilitate coupling between the models. These three variables chosen are also relevant to the mass transport model which include [CO_2], pH, and applied voltage, V_{app}.

To develop the polynomial response, we utilised Latin Hypercube Sampling (LHS) as a design of experiment (DOE) sampling method to systematically generate random 5,000 data combinations of [CO_2], pH, and V_{app} within the multidimensional parameter space as shown in Fig **S2.** The ranges for these parameters were defined in the MKM.

For each of the 5,000 data combinations obtained from LHS, additional Python scripts were written to generate their corresponding species' current densities ($\boldsymbol{J}_K$) from the microkinetic model. Linear and polynomial regression were used to establish relationships between [CO_2], pH, and V_{app}, and their corresponding current densities. These analyses were performed using the ***Scikit-Learn*** package in Python.

We determined that quadratic approximation of the polynomial response provided an optimal balance between accuracy and numerical stability for the mass transport model. Higher degree

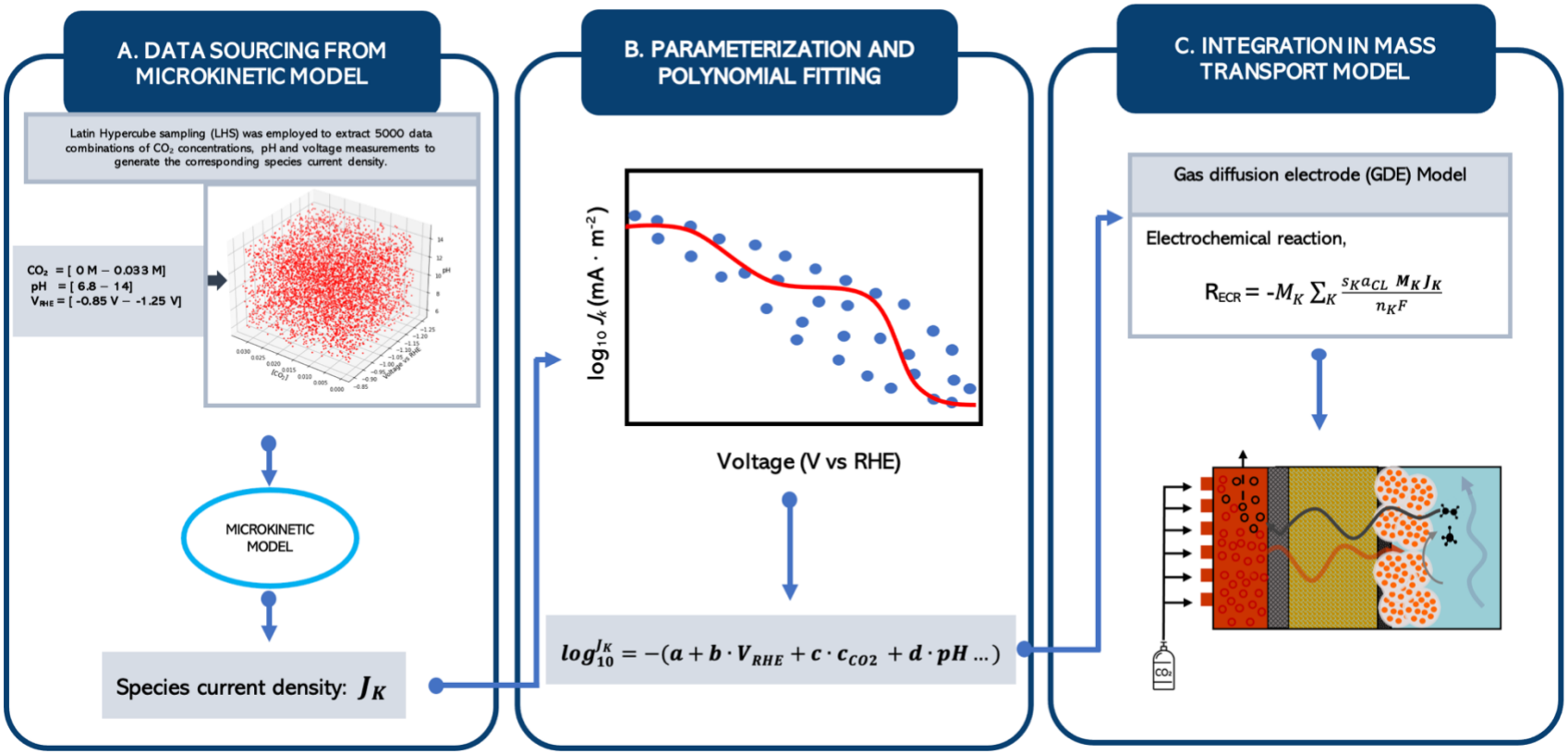

Scheme 1. (a) 5,000 data combinations of CO_2, V_{RHE} and pH generated from Latin Hypercube Sampling (LHS) fed into the calibrated microkinetic model to generate their corresponding species current density **(b)** Polynomial regression fit to species current as a function of voltage, pH and CO_2 **(c)** Integration of new polynomial species current density into GDE model for electrochemical reaction

polynomials risked overfitting the polarisation curve and introducing numerical instability, particularly in the context of COMSOL's array of PDE equations. Additionally, the natural logarithm in the initial B-Ve equation is replaced with base-10 logarithm for ease of interpretation of results.

The polynomial form of the cathodic partial current densities containing the major parameters listed earlier is given by Eq. 55.

$$log_{10}{}^{J_K} = a + b \cdot V_{app} + c \cdot c_{CO2} + d \cdot pH + e \cdot {V_{app}}^2 + f \cdot V_{app} \cdot c_{CO2} + g \cdot V_{app} \cdot pH + h \cdot {c_{CO2}}^2 + i \cdot c_{CO2} \cdot pH + j \cdot pH^2 \quad (55)$$

Values of the coefficients a – j are given in **Table S6** in the supporting information, accompanied with their coefficient of determination (R^2) and mean square error (MSE) values for the regression analysis.

The species partial current density (Eq. 55) is substituted into the electrochemical reactions, $R_{ECR,}$ given by Eq. 56 used in the mass transport GDE model.

$$R_{ECR} = -\frac{s_{j,K} \cdot a_{CL} \cdot M_K \cdot J_K}{n_K \cdot F} \quad (56)$$

The geometric current density (J_{geom}) of the *a*CL is determined by multiplying the specific surface area, *a*CL by the integration of the partial current density in Eq. 53 along the catalyst thickness on the z coordinate given by Eq. 57.

$$J_{geom} = a_{CL} \cdot \int_0^{L_{CL}} J_K \, dz \tag{57}$$

The corresponding Faradaic efficiency (FE) of the products is therefore calculated as shown in Eq. 58.

$$\text{FE} = \frac{J_K}{J_{total}} \times 100\% \tag{58}$$

2.5 **Model development in COMSOL Multiphysics**

The 1D geometry was developed in COMSOL Multiphysics 6.0, comprising two domains: GDL and *a*CL, meshed with 3.25 μm and 0.06 μm respectively. The governing equations for fluid flow and species transport were solved using MUMPS (MUltifrontal Massively Parallel Sparse Direct Solver) with relative tolerance of 0.001.

2.6 **Model Testing**

The accuracy of the developed mass transport - microkinetic GDE model was tested by comparing the simulation results to the results from the calibrated microkinetic model since the microkinetic model was originally calibrated using experimental and *ab initio* calculations. Concentrations of CO_2, pH, and V_{app} (applied voltage) are shown in **Fig. 8** alongside the current density output of the GDE (**Fig. 6**) and compared with the current densities predicted by MKM alone for the same inputs.

We chose to show model accuracy for one product from each group of products listed in Fig. **6**. These products are hydrogen gas (H_2), formate (HCOOH) and ethanol (C_2H_5OH) as illustrated in Fig **4a-c** respectively. It is observed that the current densities predicted by the mass-transport - microkinetic GDE model are comparable with those obtained from the

microkinetic model, particularly at lower current densities ranging from -0.8 to -1 V. However, discrepancies emerge at higher current densities, suggesting a deviation from the predictions of the microkinetic model.

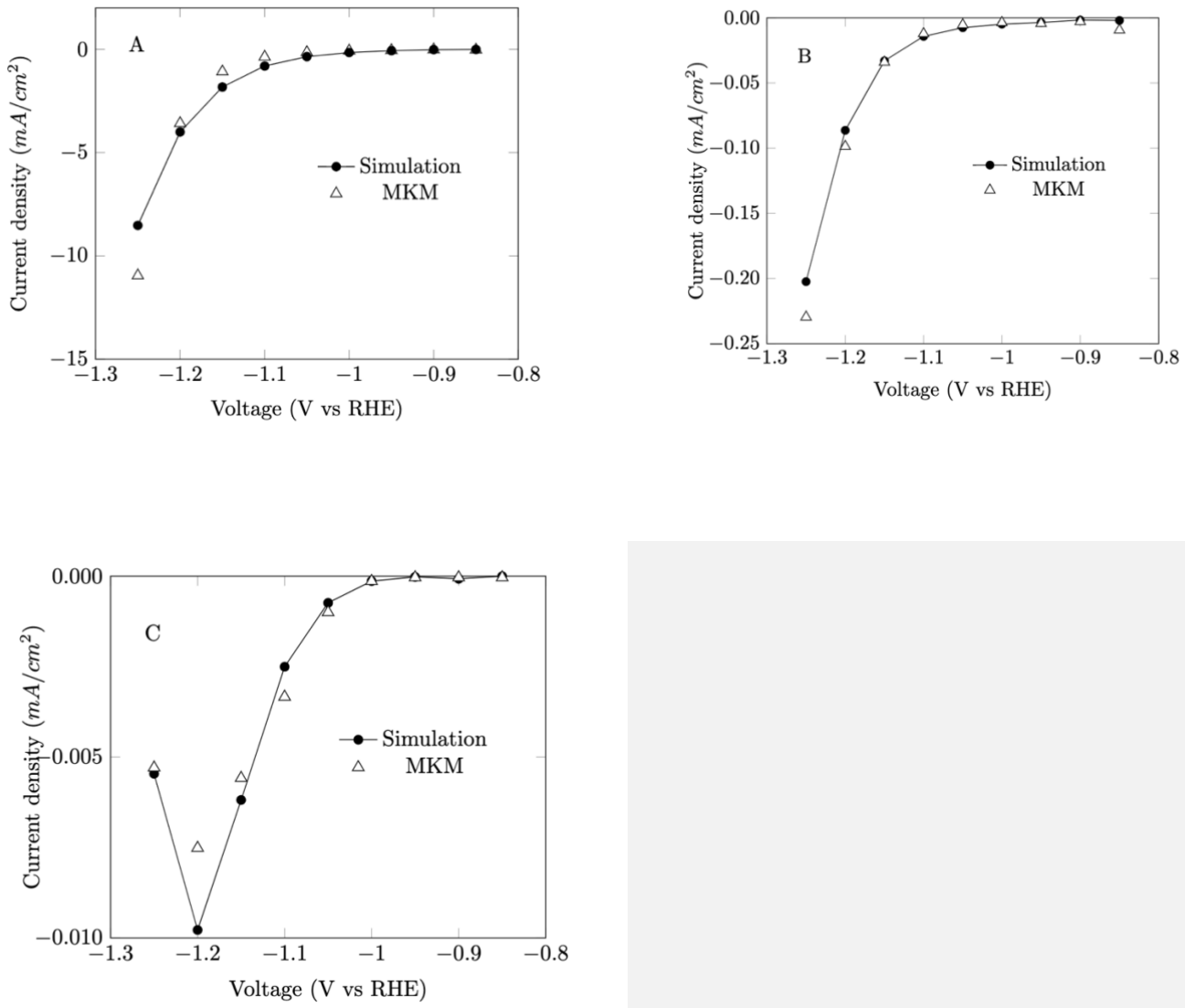

Fig. **4(a)** Simulation comparison of H_2 current density obtained from "mass transport + microkinetic model" in this work vs microkinetic model (MKM) alone. **(b)** Comparison of HCOOH current density obtained from mass transport-microkinetic model vs microkinetic

model (MKM). **(c)** Comparison of C_2H_5OH current density obtained from mass transport-microkinetic model vs microkinetic model (MKM).

This deviation between the mass transport- microkinetic model and the microkinetic model is likely attributed to the increased electrochemical activity at higher voltages, which cannot be adequately represented by quadratic polynomial approximations. Higher polynomial responses can be used to increase accuracy of the model. However, there is a risk of running into computational errors and non-convergence as a result of the combinations of partial differential equations (PDEs) used to solve the model and the higher degree polynomial (quartic or quintic approximations) for the species current density from the microkinetic model.

3. RESULTS AND DISCUSSION

3.1 Surface area, CL porosity and overlapping ratio

We modified Nafion® mass loading, which results in a change in the ratio of Cu to Nafion® loading (referred to as m_{ratio}) within the agglomerate catalyst structure. Fig **5a** shows how the CL's porosity evolves as we increase Nafion® loading. Generally, we observe a decrease in porosity as m_{ratio} decreases. The increase in Nafion® ionomer amount from 0.5 to 0.7 mg·cm^{-2} reduces the catalyst layer porosity by 50%.

Considering Nafion's® capacity for absorbing water, we find that porosity of the CL is significantly influenced by water absorption after swelling of the CL due to the presence of Nafion®, leading to a significant reduction in porosity as shown in Fig. **5a**. With increased water absorption the ionic pathways within the CL agglomerates are wetted and enhanced, while CO_2 gas transport within the CL becomes more obstructed, which influences the overall efficiency of the reaction. Apart from obstruction of $CO_{2(g)}$ transport, the active surface area is

drastically reduced, represented by the steep decline in the active surface after water saturation, as shown in Fig. **5b**.

In Fig. **5c**, an inverse relationship between the overlapping ratio and the CL porosity is observed as expected. Starting with the critical porosity which marks the onset of the catalyst overlapping, the prominence of catalyst particle overlapping intensifies as the porosity of the catalyst layer decreases below this critical threshold. The overlapping effect is particularly pronounced with an increase in the mass loading of Nafion®, leading to the formation of larger clusters from smaller agglomerates.

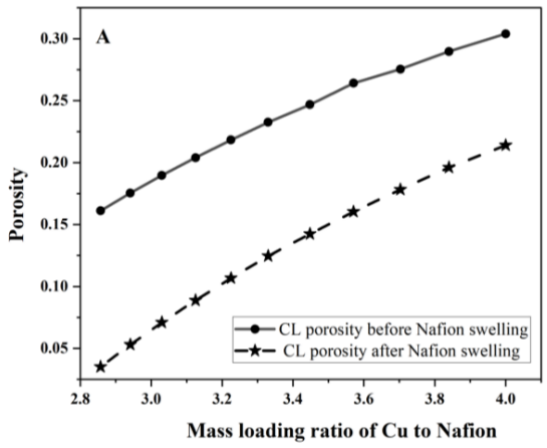

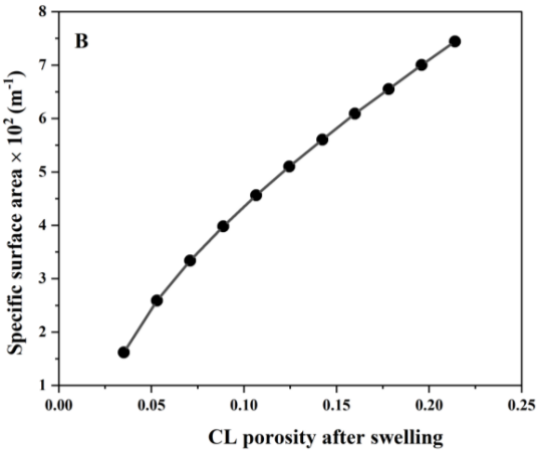

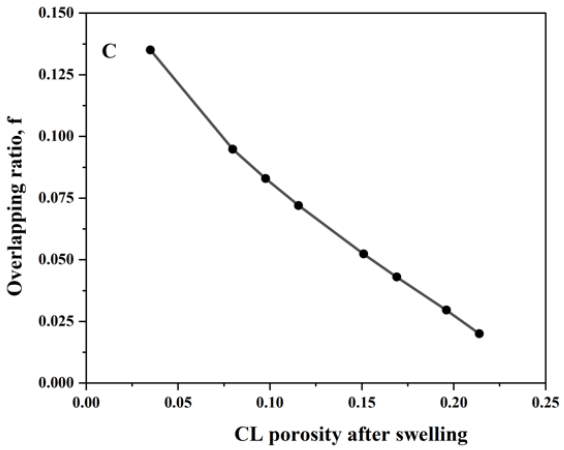

Fig. 5. (a) Porosity of the CL as a function of mass loading ratio of Cu to Nafion® before and after Nafion® swelling; **(b)** specific surface area of agglomerate as a function of CL porosity after swelling; **(c)** overlapping ratio of the agglomerates as a function of corrected CL porosity.

3.2 Product selectivity on copper catalysts

In this section, we explore how the applied voltage, CO_2 concentration and H^+ concentration (local pH) influence product selectivity on Cu(100) surface. In CO_2RR, the reaction mechanism is governed by a series of electron and proton transfers leading to specific products. Therefore, tuning the reaction landscape towards desired products involves manipulating the electrode potential (electrons) and solution pH (H^+).[47] The results discussed in this section pertain strictly to those observed on Cu(100).

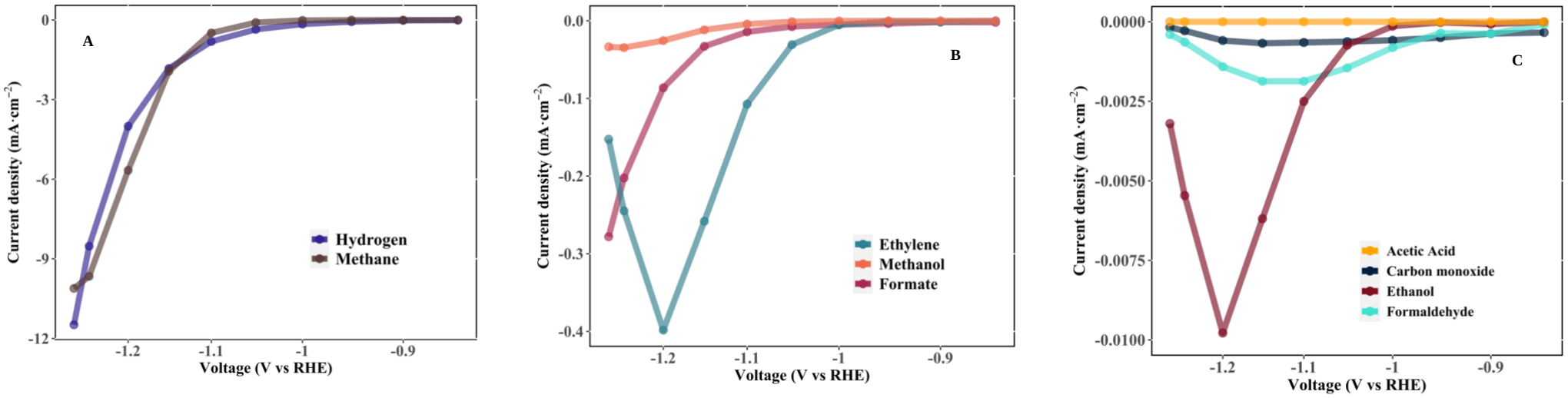

Fig. 6. Polarization curves of the simulated CO_2RR products distributed into three tiers based on the intensity of their current density. Results presented here are for m_{Cu} =2 mg cm^{-2} **and** m_{NF} = 0.5 mg cm^{-2}. **(a)** High current density products which include hydrogen (H_2) and methane (CH_4). **(b)** Medium current density (ethylene (C_2H_4), methane (CH_4), formate ($HCOO$). **(c)** Low current density (ethanol (C_2H_5OH), formaldehyde (CH_2O), carbon monoxide (CO), acetic acid (CH_3COOH)). The current densities achieved (~10 mA/cm^2) in this work are lower than typical values observed experimentally in GDE reactors due to the lower agglomerate surface area assumption used in this model.

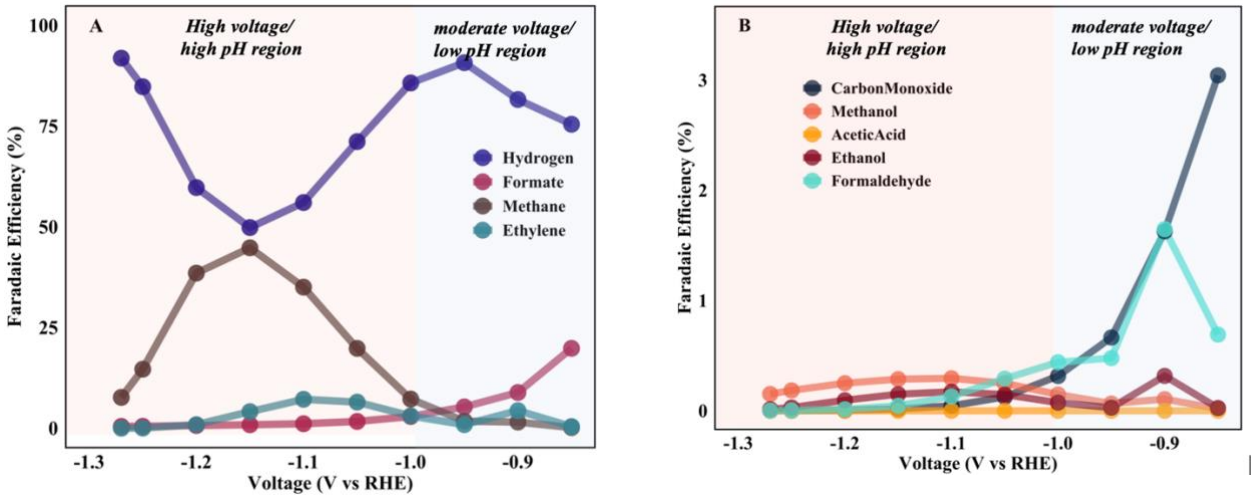

Fig. 7. Calculated Faradaic efficiencies of CO_2RR distributed into two tiers: (**a**) major products which include hydrogen (H_2), methane (CH_4), ethylene (C_2H_4) and formate ($HCOO^-$), (**b**) minor products, which include carbon monoxide (CO), ethanol (C_2H_5OH), formaldehyde (CH_2O), carbon monoxide (CO), acetic acid (CH_3COOH). Results presented here are for m_{Cu} =2 mg cm^{-2} **and** m_{NF} = 0.5 mg cm^{-2}.

a. ***Impact of applied voltage***

It is well-known that one of the key parameters that affect product distribution is the applied voltage. Electrokinetic studies on specific Cu surfaces by Hori *et al*. later expanded upon by Schouten *et al*. indicated that the mechanistic pathway on Cu(100) exhibits low voltage C2 chemistry (ethylene and ethanol) within the range of -0.4 to -0.6 V *vs* RHE, and high voltage C1/C2 chemistry (methane and ethylene) beyond -1 V *vs* RHE, as later corroborated by the work of Luo *et al*. [48–50]

The first pathway, associated with the low voltage C2 chemistry, has been demonstrated to involve a coupling reaction with no proton transfer rate determining step (i.e., pH independent), but rather an electron transfer (rate determining step of C-C coupling). In contrast, the latter pathway, corresponding to the high-voltage C1/C2 chemistry, features a pH-dependent rate-determining step (RDS) that involves the transfer of both protons and electrons.[49,50]

The applied voltage region studied in the MKM used for this work is between -0.85 V to ≈ -1.25 V which is within the moderate voltage (-0.7 V to -1.0 V) to high voltage region (> -1.0 V). Therefore, the low voltage C2 chemistry, which selectively takes place on Cu(100), is not analysed in this work since it is outside the studied voltage range. This can be expanded in future microkinetic - mass transport models when a wider range of voltages and reactant concentrations will have been investigated in a microkinetic model.

In this work, we focus on the high voltage C1/C2 pathway. Given that the electrochemical reduction of CO_2 commences with generation of formate and CO, we observe Faradaic efficiencies of these products to be higher in the medium voltage region (-0.7 to -0.9 V) as shown in Fig. **7**, with the Faradaic efficiency of formate is higher than that of CO. The relatively higher negative applied voltage within this range facilitates overcoming the initial high energy barrier ($\Delta G^{\ddagger}$=0.80 eV) for formate production as opposed to the lower barrier of 0.43 eV for CO.[44]

Meanwhile, even though the proton-electron energy barrier of CO is low, CO is consumed as it is generated since it serves as an important intermediate to produce C1 and C_{2+} products compared to formate, which is a final product. More importantly, using GDEs allows the re-adsorption of *CO intermediate along the length of the porous catalytic bed which further improves the selectivity towards C1 and C_{2+} products. This is as a result of increased surface area (compared to planar electrode) lengthening the escape route for CO. However, this effect is subject to the characteristic surface area of the GDE.[51] Towards higher negative voltages, formation of CO* becomes rate-limiting and, hence, Faradaic efficiencies of CO are almost

always low, especially at higher negative voltages with decreasing local proton concentrations in the porous catalytic bed.

One of the clear indications of moderate to high voltage region is the departure from generation of C2 products, namely ethylene and ethanol (usually produced at low voltage) with CO* hydrogenation in CHO*, towards production of methane and ethylene through the formation of hydrozymethelidyne (COH*), a key CO* hydrogenation intermediate. We observe in Figs. **6b** and **7b** that ethanol is part of the minor products generated if there are no reactant CO_2 mass transport limitations. The results also show that methane and ethylene are the major products produced after hydrogen within the high voltage region (Fig. **7a**), albeit methane is produced in larger quantities due to the relatively lower proton/electron requirement, first order dependence, and relatively lower energy barrier for methane production compared to that required for ethylene/ethanol production.[39]

Furthermore, apart from the impact of the different voltage regions, the coverage of CO* (Fig **6c** and **7b**) especially at high (negative) voltages impacts the yield of C2 products due to their second-order dependence on CO* compared to C1 products, thus contributing to lower production of ethylene and ethanol recorded at high pH values within high voltage region. This is supported by the work of Liu *et al*, also highlighting the depletion of C2 products at high voltage and high pH.[21]

On the other hand, formaldehyde (CH_2O) is observed to predominantly evolve within the lower voltage region into the medium voltage region since it shares a common intermediate of CHO* with the low-voltage C2 pathway and serves as a major reactant to produce methanol.[39] As such, methanol is also observed to have an appreciable current density competing with ethylene

and methane formation in the high voltage region due to the necessary electrode voltage of -1.12 V *vs* RHE required to produce methanol from CH_3O*.[39]

One notable pattern in the Faradaic efficiencies shown in Figs. **7a** and **7b** is the direct relationship between production of hydrocarbons (ethanol, formaldehyde, formate, ethylene) and the reduction in the production of hydrogen. As production of methane and ethylene commences at -1.0 V, hydrogen evolution diminishes, reaching a notable low Faradaic efficiency of 50%, whilst that of methane peaks at 50% at an applied voltage of -1.15 V. At higher negative voltage, production of hydrogen rises again, triggered by the lowering of production of hydrocarbons at higher voltages, partly due to the mass transport limitations of CO_2. Since this is the case, the Tafel slope of H_2 is always affected by increase or decline in the rate of production of hydrocarbons.

b. Impact of pH

pH plays a significant role in shaping the reaction microenvironment and influencing product selectivity of CO_2RR.[20,52,53] When GDEs (having a relatively higher surface area compared to planar electrodes) are operated using alkaline or buffer electrolytes such as $KHCO_3$, there is typically a rise in local pH along the length of the catalytic bed.[51] This is illustrated in Fig. **8a**. The increase in pH is a result of hydroxide ions (OH^-) being generated by consumption of CO_2 for different product species during the electrochemical reaction, see Table 1.

The extent of pH rise is dependent on RF of the catalyst, with higher surface porous catalysts producing higher surface pH due to the higher number of active sites.[51] Consequently, local pH within varies within the catalytic bed, depending on the uniformity of distribution of surface active area. The progressive variations in the local pH along the catalytic bed in mass transport models stands in contrasts with many experimental studies on the impact of pH on CO_2RR

using copper electrocatalysts. These studies typically examine impact of a discrete pH values (for example pH =1, 2, 7, 12/13) on various voltages without providing a comprehensive range of pH values on product selectivity of CO_2RR.[20,50,54] Future mechanistic models can ensure that wider ranges of pH values as a function of applied voltage are captured.

The effect of increasing local pH is observed in the logarithmic current density vs voltage plots (Fig. S3) where the relatively steeper pH rise from 7.5 at -0.9 V vs RHE to 8.7 at -0.95 V vs RHE in Figure **8** led to a corresponding change in Tafel slopes (multiple kinetic regions) and the product current densities within a CO_2 rich voltage region.

Further, it has been noted in literature that formation of ethylene on Cu(100) is pH-independent on the SHE scale but depends on local pH on the RHE scale.[20] Using highly concentrated electrolytes (such as KOH) with elevated pH has been demonstrated to significantly shift the onset voltages of ethylene and related products towards more positive values. Consequently, production of ethylene through the low voltage pathway can occur at voltage between -0.3 and -0.8 V when a higher pH (≈ 13) is used. However, our study employs a less alkaline electrolyte (0.1 $KHCO_3$) with a bulk pH of 6.8 with a low catalyst specific surface area. In the GDE mass transport model, there is a steep rise in local pH with corresponding increase in applied voltages, see Fig. **8a**. The local pH within the porous catalytic bed is therefore observed to increase to 12.5 at an applied voltage of -1.25 V due to production of OH^- ions from the electrochemical reduction of CO_2. As a result, the higher local pH required to activate formation ethylene in the low voltage C2 pathway is only achieved in the high voltage region. This leads to a significant reduction in ethylene production, as it falls outside the low voltage region for ethylene formation on Cu(100) . Therefore, even though ethylene is still produced, it is produced at a lower current density as shown in Fig. **6b**.

Experimental works such as those conducted by Schouten *et al* and Roberts *et al* investigating the influence of pH, recorded relatively lower signal of ethylene at higher pH values (pH =13) at voltages higher than -1 V.[20,54] However, specific current densities of products to illustrate the impact of different pH values on ethylene, methane and other major CO_2 products are not available.

In contrast to ethylene production, Faradaic efficiency of methane, illustrated in Fig. **7a**, exhibits an upswing in the high voltage region with the elevation of local pH in the catalytic bed. Initially, methane experiences favourable conditions in the high voltage region on Cu(100), as evidenced by various experimental studies conducted by Huang *et al.* and Roberts *et al*.[41,54] Remarkably, pH recorded in this voltage region (-1.05 to -1.15 V) aligns with the optimal local pH for methane production, ranging from 10 to 11.5.[55] Beyond this optimal pH range for methane production, as pH continues to increase, there is a decline in the current density and Faradaic efficiency of methane, paving the way for hydrogen production. This shift is notable since Cu(100) exhibits an enhanced ability to catalyse the hydrogen evolution reaction (HER).[50]

Secondly, the shorter residence time for electrochemical reduction due to the low surface area of the catalysts used in this work, promotes higher methane selectivity which is closely linked to local pH of the reaction medium.[51,55] This is also coupled with the impact of low tortuosity on low catalytic surface area as described in our previous study.[51] Low tortuosity on porous Cu electrodes shortens CO escape path, thereby reducing the local availability of CO* and inhibiting CO* re-adsorption on the catalyst for C_{2+} production. On the other hand, Hydrogen will naturally be produced around this voltage range (> -1.2 V *vs* RHE) partly due to the

intrinsic kinetics on Cu(100) facet and also the relative mass transport limitations of CO_2 around this region.

It is acknowledged that the full impact of pH and voltage cannot be comprehensively analysed in this work due to the limitations of the parameters used to calibrate the MKM. In future models, a more extensive range of applied potential, pH and temperature values can be integrated into an MKM for a thorough examination of their combined impact. It should be noted that the current densities recorded in this work are lower compared to traditional GDE models due to the lower surface area used in the model. Higher surface area will result in higher local pH which would ultimately change product distribution as a function of the applied voltage from what is observed in this work.

c. Impact of concentration of CO_2

One of the advantages of mass transport model is the ease of observing how varying concentration of reactants such as CO_2 and H^+/local pH affect product selectivity of the reaction. We observe the decline in CO_2 concentration in Fig. **8a** is subtle until -1.1 V, beyond which there is a rise in the generation of methane, ethylene, ethanol and bicarbonate ion (CO_3^{2-}) However, methane is produced in higher quantities due to the lower carbon content required.

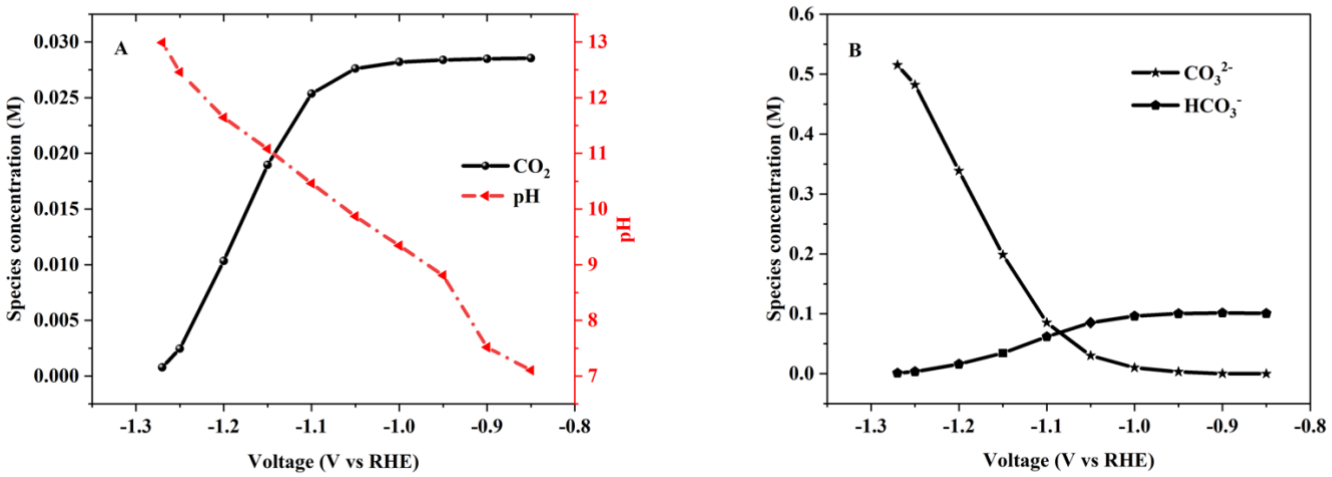

Fig. 8. Surface concentration of species as a function of voltage (RHE). (**a**) CO_2^* and local pH; (**b**) CO_3^{2-} and HCO_3^- concentrations.

Within the range of voltages, the side bicarbonate reaction competes with CO_2RR due to the rising local pH (Fig. **8a**). As availability of CO_2 is key to production of hydrocarbons on Cu electrodes, their current density is significantly affected. High concentration of bicarbonate ion recorded in this work (Fig. **8b**) is a result of the assumption of flooded agglomerates and the low surface area, which hinders efficient transport of CO_2 to reaction sites and observed low current densities of the GDE. Therefore, even though the catalytic surface area is lower which should have increased the availability of surface CO_2, the rising pH enables the parasitic bicarbonate reaction ultimately producing bicarbonates.

3.3 Advantages of mass transport – microkinetic model coupling

The results of our model in Figure 6 and 7 successfully demonstrates the capability to upscale accurate microkinetic models, capturing various elementary reactions, with gas diffusion electrode (GDE) mass transport models. In the realm of CO_2RR GDE models, we have achieved the interpretation and analysis of results through the lens of kinetics and mass

transport, which can potentially lead to the optimisation of GDE designs. The upscaling methodology offers several advantages.

One notable advantage of directly coupling mass transport to calibrated microkinetic models is the elimination of the need to describe catalytic activity using multiple Tafel slopes in cases where multiple kinetic regions are present. Consequently, there is no requirement to determine precise values of charge transfer coefficients and exchange current densities for each region, thereby simplifying the B-Ve.

Additionally, by incorporating the impact of mass transport in GDEs directly into the microkinetic model, it becomes possible to computationally optimise the reaction front within the porous catalytic bed. This optimisation is based on the parameters such as CO_2, local pH, voltage which have a direct influence on generation of desired products in the microkinetic model. The mass transport model captures crucial factors such as local pH, voltage, cation concentration, carbonate ion concentration, and operating conditions within a unified framework. We have shown how these parameters in the mass transport model can be linked with microkinetic models to investigate their impact on product distribution. The presented approach streamlines comparison of copper catalysts within the GDE development/design domain, facilitating their optimisation and contributing to the efficient scaling up of production of CO_2RR reactors.

The proposed approach removes the need to explicitly derive or assume reaction orders for species reaction with respect to CO_2 or CO, which is typical in B-Ve. Reaction orders are difficult to deduct for CO_2RR especially on Cu electrodes due to reaction complexity. The

incorporation of these considerations within the microkinetic model allows for a more integrated and comprehensive understanding of CO_2RR kinetics.

On the other hand, while it is recognised that kinetic Monte Carlo (kMC) provides a more detailed and accurate mechanistic calculation of electrode kinetics of the electrocatalytic process, its computational cost can be high due to complex lattice models employed and the numerous reaction pathways possible on Cu. This complexity has often led researchers to resort to simplified reaction pathways.[56] In comparison, the well-calibrated microkinetic models offer a moderately accurate representation of the electrode kinetics that can readily couple with mass transport models to facilitate the elucidation of the effects influencing performance of GDEs.

Furthermore, the use of polynomial equations offers flexible and straightforward framework to bridge both models without the need to solve additional complex mathematical expressions. In this work, they have been proven to effectively replace the prevailing current density typically obtained from B-Ve. Additionally, they offer a range of accuracy levels that can be optimised to prevent overfitting and ensure appropriate model fidelity. Therefore, accurate results are assured if a detailed microkinetic model of CO_2RR is developed over varying operating conditions.

4 Limitation of the model used in this work

The drawback in the methodology is the requirement of a full calibrated microkinetic model for Cu electrodes with a wide range of operating conditions such as pH, operating temperature, pressure, voltages.

In our approach, polynomial equations are used to approximate the kinetics of CO_2RR within the GDE mass transport model. While this technique ensures the incorporation of CO_2RR kinetics, there is a decrease in accuracy due to the polynomial approximations. This deviation is noticeable in the model testing process, particularly at high negative voltages, where current densities differ between the mass transport model-microkinetic model and the microkinetic model alone. Direct coupling without intermediary polynomial responses can improve the accuracy of CO_2RR kinetics. Achieving this would involve developing both mass transport and microkinetic models within the same computational software platform to facilitate seamless integration or utilising computational platforms that enable direct coupling of both models. Employing machine learning algorithms could potentially minimise the root mean squared error (RSME) of kinetic prediction, however this will require access to high-throughput experimental and computational data for model training.

Future model integration, akin to the approach outlined in this study, should aim to integrate time-dependence into both models to enhance reaction optimisation. Time-dependent models capture the transient catalyst behaviour, leading to a deeper comprehension of catalytic activity in CO_2RR on Cu electrodes. This would be beneficial for pulsed electrolysis of CO_2RR known to improve reaction selectivity and stability by inhibiting catalyst poisoning, rearrangement of surface coverage, and inhibiting the side bicarbonate reactions.[57–59]

Furthermore, recent research has observed the effect of Nafion® and solvent ink formulation on reaction pathways and product selectivity which is not accounted for in this work. Selective permeability of K^+ and H^+ and inhibition of anions OH^-, HCO_3^- and CO_3^{2-} in the Nafion®-coated Cu catalyst impacts reaction kinetics and, consequently, product selectivity of the reaction which is not captured in this work.[31,32]

5 Conclusions

The complex nature of heterogeneous catalysis on copper (Cu) electrodes for CO_2RR necessitates a careful kinetic approach. This is essential to ensure that computational models developed for gas diffusion electrodes (GDEs) accurately reflect experimental conditions and catalytic activities. We take a step forward towards direct coupling of microkinetic information over Cu electrodes with a mass transport model, to ensure almost all discovered pathways on a typical catalytic facet can be fully integrated rather than a few selected dominant pathways normally used to develop the kinetic signature of the catalyst.

In future work, efforts can be directed towards calibrating the microkinetic model across various operating conditions and structural facets of Cu especially for polycrystalline copper which makes up nanostructured catalyst used in GDEs. Additionally, the emphasis will be on incorporating the influence of diverse catalytic morphologies and interactions with the ionomer, especially as they affect product selectivity.

The core of this study centres on introducing a new methodology for computational GDE models. By bridging the gap between fundamental molecular-level processes and practical reactor design considerations, this approach enables a more comprehensive understanding of the CO_2RR process and could facilitate the optimisation of GDE designs for enhanced performance and efficiency.

DECLARATION OF COMPETING INTEREST

Authors declare no competing financial interest or personal relationship that could have appeared to influence the results reported in this paper.

CREDIT AUTHORSHIP CONTRIBUTION STATEMENT

Peace Adesina: Conceptualization, Methodology, Modelling and coupling, Writing-original draft and revisions.

Joel W Ager: Writing - reviewing and editing

Alexei Lapkin: Supervision, Funding acquisition, Writing - reviewing and editing.

ACKNOWLEDGEMENTS

P. Adesina gratefully acknowledges the joint scholarship of Cambridge Africa and Cambridge Trust for her PhD. The authors acknowledge the support of the National Research Foundation (NRF), the Prime Minister's Office, Singapore, under its Campus for Research Excellence and Technological Enterprise (CREATE) Programme through the eCO$_2$EP project, operated by the Cambridge Centre for Advanced Research and Education in Singapore (CARES) and the Berkeley Education Alliance for Research in Singapore (BEARS). The authors are grateful to Prof. Frank Marken (University of Bath) for discussion and suggestions made towards improving this work.

APPENDIX A. SUPPORTING INFORMATION.

Supplementary data related to this article can be found online at: The codes to the microkinetic model are available at https://github.com/simonrihm/cantera_eCat_MKM_CO2R.

Bibliography

1. Olah, G. A., Prakash, G. K. S. & Goeppert, A. Anthropogenic chemical carbon cycle for a sustainable future. *J. Am. Chem. Soc.* **133**, 12881–12898 (2011).

2. Huang, Z., Grim, R. G., Schaidle, J. A. & Tao, L. The economic outlook for converting CO_2 and electrons to molecules. *Energy Environ. Sci.* **14**, 3664–3678 (2021).
3. Sharifian, R., Wagterveld, R. M., Digdaya, I. A., Xiang, C. & Vermaas, D. A. Electrochemical carbon dioxide capture to close the carbon cycle. *Energy Environ. Sci.* **14**, 781–814 (2021).
4. Junge Puring, K. *et al.* Electrochemical CO_2 Reduction: Tailoring Catalyst Layers in Gas Diffusion Electrodes. *Adv. Sustain. Syst.* **5**, 1–13 (2021).
5. Weng, L.-C., Bell, A. T. & Weber, A. Z. A systematic analysis of Cu-based membrane-electrode assemblies for CO_2 reduction through multiphysics simulation. *Energy Environ. Sci.* **13**, 3592–3606 (2020).
6. Lees, E. W., Bui, J. C., Romiluyi, O., Bell, A. T. & Weber, A. Z. Exploring CO_2 reduction and crossover in membrane electrode assemblies. *Nat. Chem. Eng.* **1**, 340–353 (2024).
7. Dickinson, E. J. F. & Wain, A. J. The Butler-Volmer equation in electrochemical theory: Origins, value, and practical application. *J. Electroanal. Chem.* **872**, 114145 (2020).
8. Lukács, Z. & Kristóf, T. Determination of kinetic parameters from a new quadratic approximation of the Butler-Volmer equation. *J. Electroanal. Chem.* **918**, 116443 (2022).
9. Marcus, R. A. On the Theory of Oxidation-Reduction Reactions Involving Electron Transfer. I. *J. Chem. Phys.* **24**, 966–978 (1956).
10. Hush, N. S. Adiabatic Rate Processes at Electrodes. I. Energy-Charge Relationships. *J. Chem. Phys.* **28**, 962–972 (1958).
11. Hush, N. S. Electron transfer in retrospect and prospect 1: Adiabatic electrode processes. *J. Electroanal. Chem.* **470**, 170–195 (1999).
12. Chidsey, C. E. D. Free Energy and Temperature Dependence of Electron Transfer at the Metal-Electrolyte Interface. *Science.* **251**, 919–922 (1991).
13. Agbo, P. & Danilovic, N. An Algorithm for the Extraction of Tafel Slopes. *J. Phys. Chem. C* **123**, 30252–30264 (2019).
14. Limaye, A. M., Zeng, J. S., Willard, A. P. & Manthiram, K. Bayesian data analysis reveals no preference for cardinal Tafel slopes in CO_2 reduction electrocatalysis. *Nat. Commun.* **12**, 1–10 (2021).
15. O'Hayre, R., Cha, S.-W., Colella, W. & Prinz, F. B. *Fuel Cell Fundamentals*. (John Wiley & Sons, Inc, 2016).
16. Kuhl, K. P., Cave, E. R., Abram, D. N. & Jaramillo, T. F. New insights into the electrochemical reduction of carbon dioxide on metallic copper surfaces. *Energy Environ. Sci.* **5**, 7050–7059 (2012).
17. Kortlever, R., Shen, J., Schouten, K. J. P., Calle-Vallejo, F. & Koper, M. T. M. Catalysts and Reaction Pathways for the Electrochemical Reduction of Carbon Dioxide. *J. Phys. Chem. Lett.* **6**, 4073–4082 (2015).
18. Huang, Y., Handoko, A. D., Hirunsit, P. & Yeo, B. S. Electrochemical Reduction of CO_2 Using Copper Single-Crystal Surfaces: Effects of $CO*$ Coverage on the Selective Formation of Ethylene. *ACS Catal.* **7**, 1749–1756 (2017).
19. Nie, X., Luo, W., Janik, M. J. & Asthagiri, A. Reaction mechanisms of CO_2 electrochemical reduction on Cu(1 1 1) determined with density functional theory. *J. Catal.* **312**, 108–122 (2014).
20. Schouten, K. J. P., Pérez Gallent, E. & Koper, M. T. M. The influence of pH on the reduction of CO and CO_2 to hydrocarbons on copper electrodes. *J. Electroanal. Chem.* **716**, 53–57 (2014).

21. Liu, X. *et al.* pH effects on the electrochemical reduction of CO_2 towards C2 products on stepped copper. *Nat. Commun.* **10,** 32, (2019).
22. Kim, Y. G. *et al.* Surface reconstruction of pure-Cu single-crystal electrodes under CO-reduction potentials in alkaline solutions: A study by seriatim ECSTM-DEMS. *J. Electroanal. Chem.* **780**, 290–295 (2016).
23. Min, S. *et al.* Low overpotential and high current CO_2 reduction with surface reconstructed Cu foam electrodes. *Nano Energy* **27**, 121–129 (2016).
24. Shinagawa, T., Garcia-Esparza, A. T. & Takanabe, K. Insight on Tafel slopes from a microkinetic analysis of aqueous electrocatalysis for energy conversion. *Sci. Rep.* **5**, 23955–6900 (2015).
25. Li, W. *et al.* Lowering C−C coupling barriers for efficient electrochemical CO_2 reduction to C2H4 by jointly engineering single Bi atoms and oxygen vacancies on CuO. *Appl. Catal. B Environ.* **318**, 121823 (2022).
26. Pei, Y., Zhong, H. & Jin, F. A brief review of electrocatalytic reduction of CO_2—Materials, reaction conditions, and devices. *Energy Sci. Eng.* **9**, 1012–1032 (2021).
27. Motagamwala, A. H. & Dumesic, J. A. Microkinetic Modeling: A Tool for Rational Catalyst Design. *Chem. Rev.* **121**, 1049–1076 (2021).
28. Rihm, S. D. *et al.* Modelling a detailed kinetic mechanism for electrocatalytic reduction of CO_2. *Proc. Combust. Inst.* **39**, 5647–5655 (2023).
29. Bohra, D., Chaudhry, J. H., Burdyny, T., Pidko, E. A. & Smith, W. A. Mass transport in catalytic pores of GDE-based CO_2 electroreduction systems. *ChemRxiv. Prepr.* DOI: 10.26434/chemrxiv.13073348.v1 (2020).
30. Kim, C. *et al.* Tailored catalyst microenvironments for CO_2 electroreduction to multicarbon products on copper using bilayer ionomer coatings. *Nat. Energy* **6**, 1026–1034 (2021).
31. Adesina, P., Elliott, J. & Lapkin, A. Multiscale modelling of species transport in hydrophilic Nafion®-coated Cu catalysts for CO_2 electro-reduction. *Chem. Eng. J.* **478**, 147461 (2023).
32. De Sousa, L., Harmoko, C., Benes, N. & Mul, G. Optimizing the Ink Formulation for Preparation of Cu-Based Gas Diffusion Electrodes Yielding Ethylene in Electroreduction of CO_2. **1**, 1649–1658 (2021).
33. Ding, P. *et al.* Elucidating the Roles of Nafion/Solvent Formulations in Copper-Catalyzed CO_2 Electrolysis. *ACS Catal.* **13**, 5336–5347 (2023).
34. Xing, L. An agglomerate model for PEM fuel cells operated with non-precious carbon-based ORR catalysts. *Chem. Eng. Sci.* **179**, 198–213 (2018).
35. Cetinbas, F. C., Advani, S. G. & Prasad, A. K. An Improved Agglomerate Model for the PEM Catalyst Layer with Accurate Effective Surface Area Calculation Based on the Sphere-Packing Approach. *J. Electrochem. Soc.* **161**, F803–F813 (2014).
36. Maestri, M. Escaping the trap of complication and complexity in multiscale microkinetic modelling of heterogeneous catalytic processes. *Chem. Commun* **53**, 10244 (2017).
37. Ringe, S. *et al.* Double layer charging driven carbon dioxide adsorption limits the rate of electrochemical carbon dioxide reduction on Gold. *Nat. Commun.* **11**, (2020).
38. Govindarajan, N., Lin, T. Y., Roy, T., Hahn, C. & Varley, J. B. Coupling Microkinetics with Continuum Transport Models to Understand Electrochemical CO_2 Reduction in Flow Reactors. *PRX ENERGY* **2**, 33010 (2023).
39. Luo, W., Nie, X., Janik, M. J. & Asthagiri, A. Facet Dependence of CO_2 Reduction Paths on Cu Electrodes. *ACS Catal.* **6**, 219–229 (2016).
40. Luc, W. *et al.* Two-dimensional copper nanosheets for electrochemical reduction of carbon monoxide to acetate. *Nat. Catal.* **2**, 423–430 (2019).

41. Huang, Y., Handoko, A. D., Hirunsit, P. & Yeo, B. S. Electrochemical Reduction of CO2 Using Copper Single-Crystal Surfaces: Effects of CO∗ Coverage on the Selective Formation of Ethylene. *ACS Catal.* **7**, 1749–1756 (2017).
42. Montoya, J. H., Shi, C., Chan, K. & Nørskov, J. K. Theoretical Insights into a CO Dimerization Mechanism in CO_2 Electroreduction. *J. Phys. Chem. Lett.* **6**, 2032–2037 (2015).
43. Goodpaster, J. D., Bell, A. T. & Head-Gordon, M. Identification of Possible Pathways for C−C Bond Formation during Electrochemical Reduction of CO_2: New Theoretical Insights from an Improved Electrochemical Model. *J. Phys. Chem. Lett* **7**, 45 (2016).
44. Cheng, T., Xiao, H. & Goddard, W. A. Full atomistic reaction mechanism with kinetics for CO reduction on Cu(100) from ab initio molecular dynamics free-energy calculations at 298 K. *Proc. Natl. Acad. Sci. U. S. A.* **114**, 1795–1800 (2017).
45. Calle-Vallejo, F. & Koper, M. T. M. Theoretical considerations on the electroreduction of CO to C2 Species on Cu(100) electrodes. *Angew. Chemie - Int. Ed.* **52**, 7282–7285 (2013).
46. Philip, M., Woldu, A. R., Akbar, M. B., Louis, H. & Cong, H. A facile synthesis of Cu catalysts with multiple high-index facets for the suppression of competing H2evolution during electrocatalytic CO_2 reduction. *Nanoscale* **13**, 3042–3048 (2021).
47. Xiang, S. Q., Gao, S. T., Shi, J. L., Zhang, W. & Zhao, L. Bin. Developing micro-kinetic model for electrocatalytic reduction of carbon dioxide on copper electrode. *J. Catal.* **393**, 11–19 (2021).
48. Hori, Y., Takahashi, I., Koga, O. & Hoshi, N. Electrochemical reduction of carbon dioxide at various series of copper single crystal electrodes. *J. Mol. Catal. A Chem.* **199**, 39–47 (2003).
49. Schouten, K. J. P., Kwon, Y., Van Der Ham, C. J. M., Qin, Z. & Koper, M. T. M. A new mechanism for the selectivity to C1 and C2 species in the electrochemical reduction of carbon dioxide on copper electrodes. *Chem. Sci.* **2**, 1902–1909 (2011).
50. Schouten, K. J. P., Qin, Z., Gallent, E. P. & Koper, M. T. M. Two pathways for the formation of ethylene in CO reduction on single-crystal copper electrodes. *J. Am. Chem. Soc.* **134**, 9864–9867 (2012).
51. Liu, G. *et al.* Elucidating Reaction Pathways of the CO_2 Electroreduction via Tailorable Tortuosities and Oxidation States of Cu Nanostructures. *Adv. Funct. Mater.* **32**, 2204993 (2022).
52. Hori, Y., Takahashi, R., Yoshinami, Y. & Murata, A. Electrochemical reduction of CO at a copper electrode. *J. Phys. Chem. B* **101**, 7075–7081 (1997).
53. Varela, A. S. The importance of pH in controlling the selectivity of the electrochemical CO_2 reduction. *Current Opinion in Green and Sustainable Chemistry*, **26**, 100371 (2020).
54. Roberts, F. S., Kuhl, K. P. & Nilsson, A. Electroreduction of Carbon Monoxide over a Copper Nanocube Catalyst: Surface Structure and pH Dependence on Selectivity. *ChemCatChem* **8**, 1119–1124 (2016).
55. Obasanjo, C. A. *et al.* High-rate and selective conversion of CO_2 from aqueous solutions to hydrocarbons. *Nat. Commun.* **14**, 1–12 (2023).
56. Li, J., Maresi, I., Lum, Y. & Ager, J. W. Effects of surface diffusion in electrocatalytic CO_2 reduction on Cu revealed by kinetic Monte Carlo simulations. *J. Chem. Phys.* **155**, (2021).
57. Shiratsuchi, R., Aikoh, Y. & Nogami, G. Pulsed Electroreduction of CO_2 on Copper Electrodes. *J. Electrochem. Soc.* **140**, 3479–3482 (1993).
58. Casebolt, R., Levine, K., Suntivich, J. & Hanrath, T. Pulse check: Potential opportunities in pulsed electrochemical CO_2 reduction. *Joule* **5**, 1987–2026 (2021).

59. Lim, C. F. C., Harrington, D. A. & Marshall, A. T. Altering the selectivity of galvanostatic CO_2 reduction on Cu cathodes by periodic cyclic voltammetry and potentiostatic steps. *Electrochim. Acta* **222**, 133–140 (2016).